Optical Engineering

OpticalEngineering.SPIEDigitalLibrary.org

Double and triple-wavelength plasmonic demultiplexers based on improved circular nanodisk resonators

Shiva Khani
Mohammad Danaie
Pejman Rezaei

Shiva Khani, Mohammad Danaie, Pejman Rezaei, "Double and triple-wavelength plasmonic demultiplexers based on improved circular nanodisk resonators," *Opt. Eng.* **57**(10), 107102 (2018), doi: 10.1117/1.OE.57.10.107102.

Optical Engineering 57(10), 107102 (October 2018)

Double and triple-wavelength plasmonic demultiplexers based on improved circular nanodisk resonators

Shiva Khani, Mohammad Danaie,* and Pejman Rezaei
Semnan University, Electrical and Computer Engineering Faculty, Semnan, Iran

Abstract. Plasmonic demultiplexers using improved circular nanodisk resonators (CNRs) and metal-insulator-metal waveguides have been designed. The proposed structures use air and silver as insulator and metal layers, respectively. The relative permittivity of silver has been characterized by Drude, Palik, and Drude–Lorentz models in our finite-difference time-domain simulations. To obtain demultiplexers, first two filters based on improved CNRs are designed. One of the most outstanding features of a CNR is that the resonance wavelength can be tuned by changing its radius. It is shown that increasing the CNRs radii for the single-mode bandpass filter increases the resonance wavelength, linearly. Accordingly, double and triple-wavelength demultiplexers (DeMuxes) have been proposed for the wavelength range of 600 to 2000 nm. Due to their small area, the proposed demultiplexers can be applied in integrated optical circuits for optical communication purposes. [DOI: 10.1117/1.OE.57.10.107102]

Keywords: plasmonic demultiplexer; metal-insulator-metal waveguide; circular nanodisk resonator; Drude–Lorentz model; finite-difference time-domain method.

Paper 181028 received Jul. 15, 2018; accepted for publication Sep. 18, 2018; published online Oct. 16, 2018.

1 Introduction

Electromagnetic waves that propagate at a metal–dielectric interface are known as surface plasmon polaritons (SPPs). Due to their ability to overcome the diffraction limit and manipulate light for deep subwavelength scales, SSPs are extensively studied nowadays.[1,2] Because of the relatively large size of the traditional optical devices such as photonic crystal (PhC) switches,[3] filters,[4,5] splitters,[6] optical memories[7] sensors,[8] full-adders,[9] and slow-light waveguides,[10] they are not the perfect choice for future ultracompact photonic-integrated circuits.[11,12] Many metal-insulator-metal (MIM) plasmonic devices based on SPPs have been recently introduced. Some of them include: plasmonic filters,[13–16] sensors,[17–20] splitters,[21,22] switches,[23–25] modulators,[26,27] slow-light waveguides,[28] and bit magnitude comparators.[29]

Due to the vast attention and interest to optical demultiplexers (DeMuxes), a huge amount of studies have been directed on their realization. Using PhC structures, different optical DeMuxes have already been designed.[30–35] Ring resonators are one of the main resonators used to design PhC DeMuxes. A benefit of using PhC setups for realization of these devices is that very sharp optical filters can be designed and implemented using PhCs. Such sharp filters can increase the number of channels in an optical DeMux. Furthermore, PhCs filters can have near negligible absorptions, which is a very important advantage. As a result, there are many different types of PhC Demuxes reported in the literature. Using PhC ring resonators, four-channel[30–33] and six-channel[34] DeMuxes have been proposed. Also, a three-channel DeMux using ring resonators in triangular PhC has been designed in Ref. 35. But as previously mentioned, PhC devices occupy much more area than MIM plasmonic structures. Due to the small footprint of plasmonic devices, they seem a good choice for highly integrated optical devices. As a result, plasmonic DeMuxes are recently being under consideration.

To design an optical DeMux, the first step is design optical bandpass filters (BPFs). To design BPFs, one solution is to design a cavity with a tunable resonance wavelength. If such a cavity is side-coupled to two waveguides with a mode-profile similar to the resonance profile of the cavity, a BPF can be created.[7] To have a DeMux, different BPFs with different resonances have to be joined together via an input bus waveguide. When an optical signal is inserted to the bus waveguide, the frequency components of the signals excite different cavities. Each cavity leaks the corresponding frequency components to its respective output waveguide, which results in their separation.

Plasmonic DeMuxes owing to their important role in wavelength division multiplexing systems have found wide application in optical systems. Using DeMuxes, two or more wavelengths can be separated from each other and transmitted to multiple output ports. Various structures and resonator configurations have been recently introduced for plasmonic DeMuxes.[36–53] One of the most common types of resonators used to design DeMuxes is circular nanodisk resonator (CNR). CNRs have desirable properties such as easy implementation and tunable resonance frequency. Accordingly, different DeMux structures have been designed based on such resonators. The resonance frequency of CNRs can be easily tuned by changing the CNR radius. Such a method is used in Refs. 36 and 37 for designing DeMuxes. Another idea that has been used to design different DeMux structures based on CNRs is to change the refractive index of CNRs.[38,39]

Ring resonators have also been suggested to design DeMuxes. Dual wavelength DeMuxes using circular ring resonator and square ring resonator have been reported in Refs. 40 and 41, respectively. In Ref. 42, in addition to using

---

*Address all correspondence to: Mohammad Danaie, E-mail: danaie@semnan.ac.ir

the ring resonator, the MIM waveguide is also designed in the form of a ring shape. The DeMux size can be reduced using such a method. In Ref. 43, by coupling waveguide bends, numerous structures including a multiplexer (Mux), a DeMux, and a power splitter are designed. In addition to the previous method, by changing the cavity shape, the DeMux structures can be further improved. Square cavities and rectangular cavities are suggested to design plasmonic DeMuxes in Refs. 44–47. Other approaches, such as plasmonic DeMuxes employing tapered structures,[48,49] hexagonal resonators,[50] H-shaped resonators,[51] Y-bent plasmonic waveguides with square cavities,[52] and teeth-shaped waveguide structures,[53] have also been proposed.

The advantage of MIM structures is that they can be integrated with other electrical circuits on a single chip. Accordingly, they are already used for designing of microwave circuits. Such microwave circuits include microstip filters,[54–57] Muxes,[58,59] antennas,[60,61] etc. The models that are currently used for the characterization of metal layers in finite-difference time-domain (FDTD) simulations of plasmonic devices are Drude or plasma, Palik, and Drude–Lorentz models (DLMs). Among the mentioned models, the Drude model is the most approximated model which is used in most studies. The results obtained from the Drude model are not always reliable.[62,63] Accordingly, it is better that more accurate models such as Palik or DLMs be used for the characterization of metal layers. Here, the three models are compared for the filter structures to provide a better insight.

In this paper, using improved CNRs, several plasmonic DeMux structures are proposed. CNR is one of the mostly used resonator topologies for plasmonic filters and DeMuxes designing. A regular CNR generates two resonance modes, which complicates DeMux designing. It is more desirable to use a single-mode resonator for design of a multichannel DeMux. Hence, the CNR is first transformed to a single-mode resonator using two symmetric and asymmetric parenthesis-shaped structures.[13] Thereafter, using the two improved CNRs three dual-wavelength and two triple-wavelength DeMuxes are designed for selecting different wavelengths. All of the proposed DeMux structures are simulated using Drude and DLMs. The main advantages of the proposed structures are using single-mode resonators and having high transmittance peaks.

2 Single-Mode Bandpass Filter Design Procedure

The topology of the initial BPF and the improved BPFs (filter A and filter B) that are used in this paper are shown in Fig. 1. The initial filter is composed of two waveguides and a CNR between them. Its dimensions are as follows: $w = 50$ nm, $r = 310$ nm, and $g = 16$ nm. Having a single-mode resonator is much more helpful for DeMux designing. As a result, using two symmetric and asymmetric parenthesis shaped structures, two types of single-mode plasmonic filters are designed. The dimensions of filter "A" and "B" are as follows: $w = 50$ nm, $r_1 = r_2 = 310$ nm, $r_{i1} = r_{i2} = 326$ nm, $r_{o1} = r_{o2} = 376$ nm, $g_1 = g_2 = 16$ nm, $\theta_1 = \theta_2 = 75$ deg, and $\alpha = 22$ deg. The insulator and metal parts of the structures (white and blue areas) are assumed to be air and silver with the relative permittivity of $\varepsilon_d = 1$ and ε_m, respectively. The value of ε_m is the frequency-dependent, which is characterized by Drude, Palik, and DLMs. Hence, three models are initially defined.

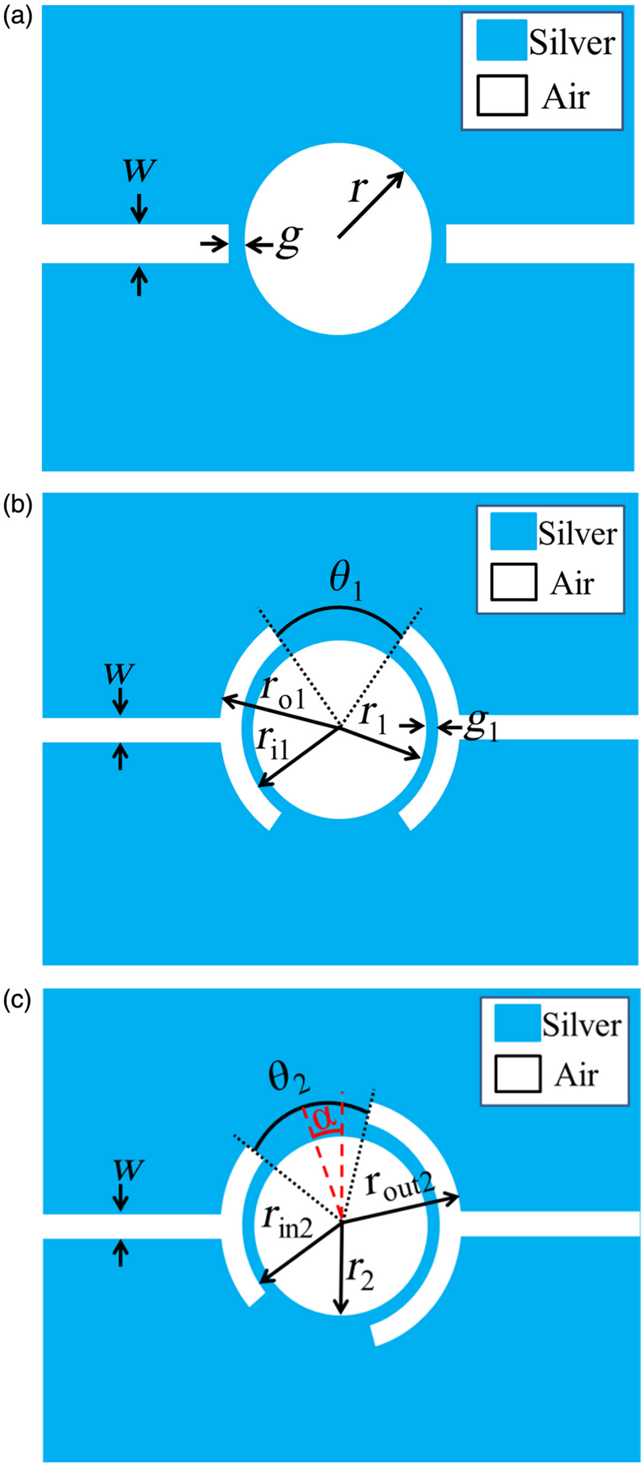

Fig. 1 (a) Initial plasmonic BPF topology (b) filter A and (c) filter B.

The model that is used in most studies reported in the literature is the Drude model. Using Eq. (1), the Drude model can be expressed as follows:[64]

$$\varepsilon_m(\omega) = \varepsilon_\infty - \frac{\omega_p^2}{\omega(\omega + j\gamma)}, \tag{1}$$

where $\varepsilon_\infty = 3.7$ is the dielectric permittivity at the infinite frequency, $\gamma = 0.081$ ev is the electron collision frequency, $\omega_p = 9.1$ ev is the bulk plasma frequency of silver, and ω is the angular frequency of incident light. As can be seen from Eq. (1), the Drude model uses a very simplistic approximation and cannot always be a trustworthy model for FDTD simulations. Another model that is much more accurate for the characterization of the silver is the Palik model. This model is valid over a wider wavelength range. It has been described in Ref. 63. The last model that has been introduced here is the DLM. The relative permittivity of the seven-pole DLM is as follows:

$$\varepsilon_m(\omega) = 1 - \frac{\omega_p^2}{\omega(\omega + j\gamma)} + \sum_{n=1}^{5} \frac{f_n \omega_n^2}{\omega_n^2 - \omega^2 - j\omega\gamma_n}. \tag{2}$$

In this model, $\omega_p = 2002.6$ THz and $\gamma = 11.61$ THz are the bulk plasma frequencies of silver and the damping constant, respectively. Also, ω_n represents the resonant frequency, γ_n is damping constant, and f_n is oscillators' strength. The values of ω_n, γ_n and f_n are given in Table 1.

The real and imaginary parts of the permittivity of the Drude, Palik, and DLMs are shown in Fig. 2. In this figure, the real and imaginary parts of the permittivity of the Drude and DLMs have been calculated using Eqs. (1) and (2), and the experimental data of the Palik model has been used to draw the real and imaginary parts of its permittivity. The black lines represent the real parts and the red lines denote the imaginary parts of the permittivity of three models. As can be seen from Fig. 2, the permittivity of the Palik and DLMs, which are more accurate models, is almost similar for wavelengths lower than 1500 nm. But the permittivity of the Drude model is slightly different from the Palik and DLMs. Therefore, it is expected that the transmission spectra using the Palik and DLMs are more similar.

Table 1 Parameters of the Drude–Lorentz model for silver.

n	ω_n (THz)	γ_n (THz)	f_n
1	197.3	939.62	7.9247
2	1083.5	109.29	0.5013
3	1979.1	15.71	0.0133
4	4392.5	221.49	0.8266
5	9812.1	584.91	1.1133

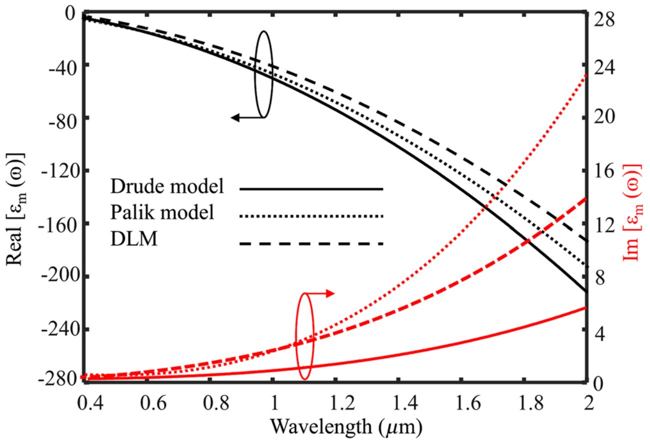

Fig. 2 Real and imaginary parts of the silver permittivity using three models.

Figure 3 compares the FDTD simulation transmission spectra of the BPFs using Drude, Palik, and DLMs and shows the accuracy of the Palik and DLMs. As shown in this figure, the initial plasmonic BPF generates two resonance modes (modes 1 and 2). The conventional CNR has been used to design DeMuxes in the most studies. Such a structure is not desirable for multichannel DeMuxes due to having two resonance modes. Therefore, single-mode resonators have to be designed first.[13] The maximum transmission peak values

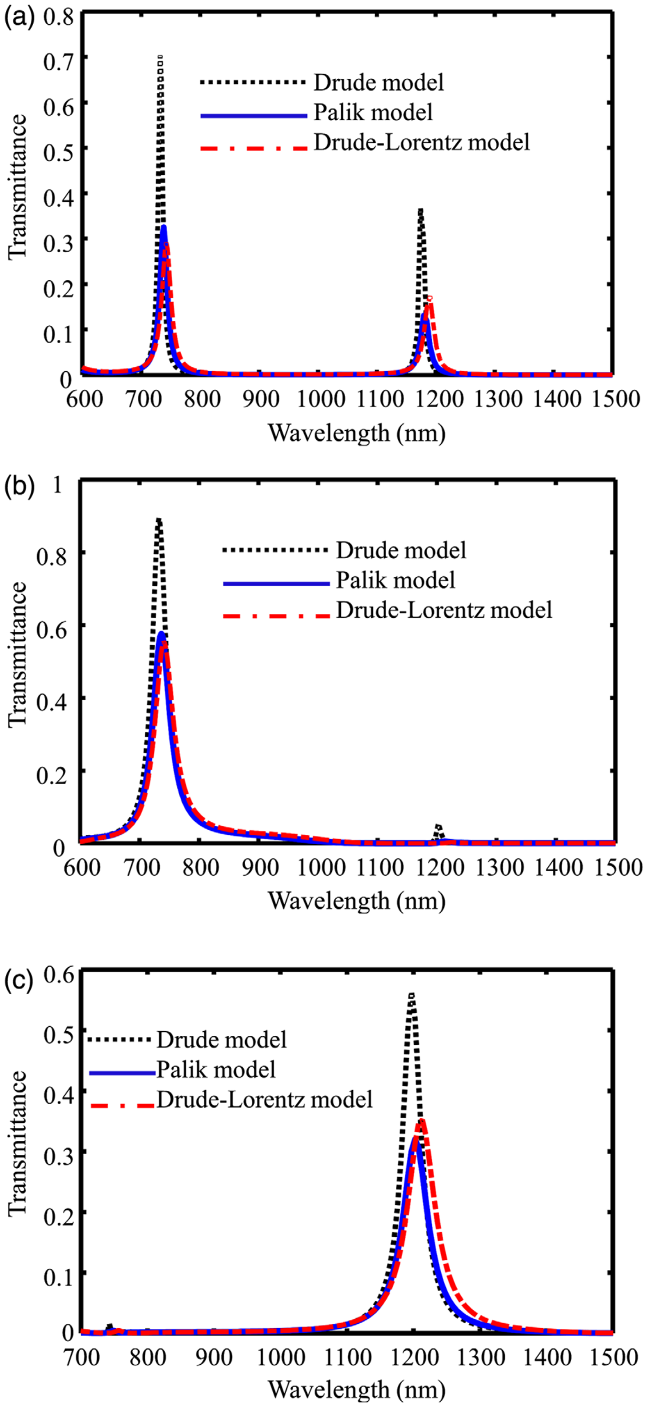

Fig. 3 Transmission spectrum of (a) initial filter, (b) filter A, and (c) filter B.

for Drude model are much higher than the Palik and DLMs for all three filters.

As seen from Eq. (1), the Drude model formula for permittivity of silver is quite simplistic. For this reason, the FDTD simulation results for transmission spectra that are obtained using the Drude model are less reliable. But the DLM's permittivity formula of silver [Eq. (2)] is more complex than the Drude model formula, which increases the accuracy of such a model. As seen from Fig. 2, the real and imaginary parts of the permittivity of the Palik model is also similar to the DLM. Accordingly, the transmission spectra of the filters using accurate Palik and DLMs are very similar. Therefore, because of the approximation in the Drude permittivity formula, the transmission spectra in resonance modes are higher than other two accurate models. As can be seen from Figs. 3(b) and 3(c), filters A and B have a higher transmittance compared with the initial structure.

As already mentioned, one of the advantages of the CNR is that the resonance wavelength can be tuned by changing its radius and dielectric material. The reason can be explained based on[65–67]

$$K_d \frac{H_n'^{(1)}(K_m r)}{H_n^{(1)}(K_m r)} = K_m \frac{J_n'(K_d r)}{J_n(K_d r)}, \tag{3}$$

$$K_d = K(\varepsilon_d)^{1/2}, \tag{4}$$

$$K_m = K(\varepsilon_m)^{1/2}. \tag{5}$$

In these formulae, K_d and K_m represent the wave vectors in the dielectric and metal CNR, respectively. K is the wave number and r is the CNR radius. ε_m and ε_d are the relative dielectric constants of the metal and dielectric, respectively. $H_n^{(1)}$ is the first kind Hankel function of the order n and J_n is the first kind Bessel function of the order n. $H_n'^{(1)}$ and J_n' are the Hankel function and Bessel function derivatives, respectively. It can be seen from Eq. (3) that the resonance wavelengths of a CNR depend on r and $\varepsilon_d^{1/2}$, respectivley.

It is expected for the resonance wavelength to increase as the radius is increased. The reason can be explained according to Eq. (3), which shows the resonance condition. Assume that for a certain radius "r," the left and the right sides of the equation are equal. Such a radius satisfies the resonance condition. As seen, the argument of the Bessel and Hankel function is the product of K, $\sqrt{\varepsilon}$, and r parameters. Imagine that the value of r has been increased to r_1. Assuming that ε remains the same, for the argument value to remain constant, K has to be decreased (so as to make up for the increment of the radius and still keep the left side and the right side of the equation in an equilibrium). As K is inversely related to the wavelength, the resonance wavelength has to be increased.

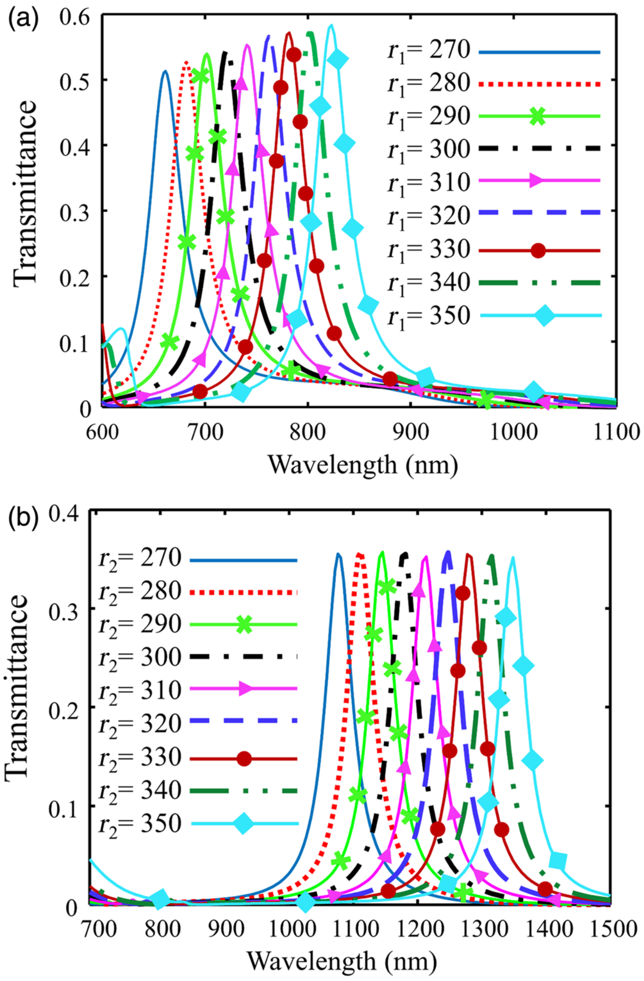

Fig. 4 Transmission spectrum for different values of radius for (a) filter A and (b) filter B.

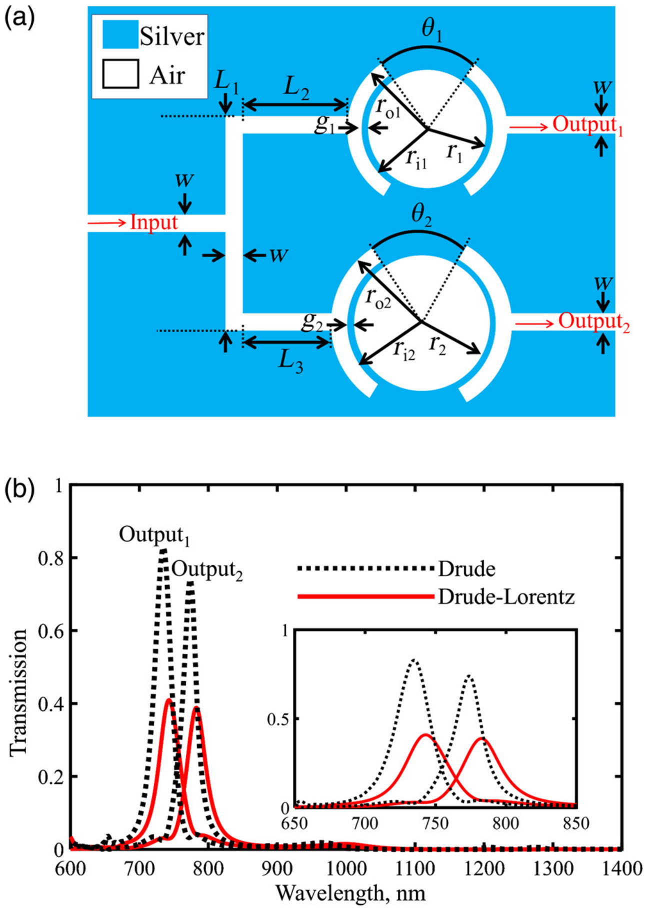

Fig. 5 (a) DeMux1 topology and (b) its transmission spectra.

As a result, an increase in the radius increases the resonance wavelength.

The transmission spectra of two proposed single-mode filters for different values of CNR radii are shown in Fig. 4. As seen, by increasing the CNR radii from 270 to 350 nm, the resonance wavelengths are shifted to higher wavelengths. Hence, by coupling CNRs with diverse radii to a central waveguide, multichannel DeMuxes can be formed. Having a single-mode filter simplifies the DeMuxes design procedure.

3 Double-Wavelength DeMuxes Design Procedure

Two single-mode plasmonic BPFs were proposed in the previous section. As already mentioned, a single-mode filter plays an important role for designing multichannel DeMuxes. The two-channel DeMuxes are realized by adding an extra channel with different CNR radii. Here, three double-wavelength DeMux structures (for different wavelength regions) are designed using the mentioned method. Figure 5(a) shows a two-channel DeMux topology based on filter A (DeMux1). The proposed structure is composed of two improved CNRs (a CNR with symmetric parenthesis-shaped structures) with different dimensions. The design parameters are as follows: $r_1 = 310$ nm, $r_2 = 330$ nm, $r_{i1} = 326$ nm, $r_{i2} = 346$ nm, $r_{o1} = 376$ nm, $r_{o2} = 396$ nm, $g_1 = g_2 = 16$ nm, $\theta_1 = \theta_2 = 75$ deg, $w = 50$ nm, $L_1 = 950$ nm, $L_2 = 200$ nm, and $L_3 = 180$ nm. The transmission spectra of two outputs of DeMux1 using Drude and DLMs are shown in Fig. 5(b). Based on the theoretical analysis mentioned before, the resonance wavelength is linearly related to the CNR radius. The resonance wavelengths of two outputs (output_1 and output_2) using the DLM are 742 and 782 nm with maximum transmission peaks of 41% and 37%, respectively. It is shown that the obtained resonance wavelengths using the Drude model are almost equal to DLM ($\lambda_1 = 734$ and $\lambda_2 = 774$ nm), whereas the maximum transmission peaks of them are significantly increased. The maximum transmission peaks of the first and second output resonance wavelengths using the Drude model are 83% and 74%, respectively. As can be seen from the transmission spectra of the improved filters [Figs. 3(b) and 3(c)], filters A and B pass the second mode (lower resonance wavelength) and first mode (higher resonance wavelength) of the initial filter, respectively. Accordingly, DeMux1, which is created using filter A, generates two output resonance wavelengths at the lower wavelengths range.

For a better insight, the field profile of H_Z magnitude for two wavelengths of DLM ($\lambda_1 = 742$ and $\lambda_2 = 782$ nm) is also shown in Fig. 6. It can be seen that the resonance wavelength of $\lambda_1 = 742$ nm is coupled to the upper CNR and is transmitted to the output_1 port, whereas output_2 transmits the wavelength of $\lambda_2 = 782$ nm. The resonance profiles depend

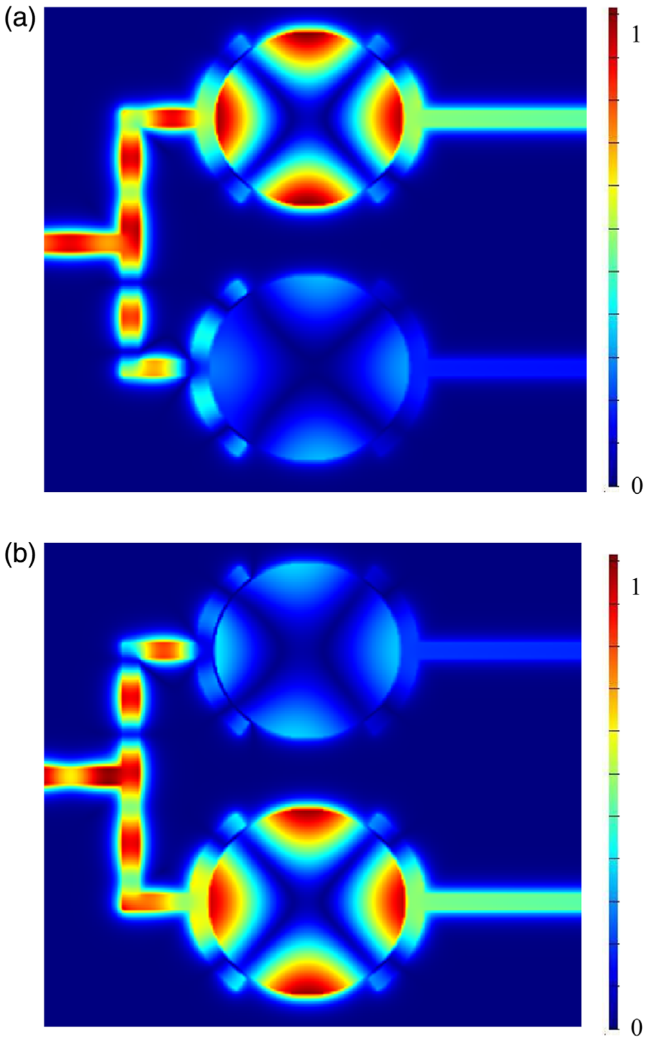

Fig. 6 Field profile of H_Z magnitude of DeMux1 for wavelengths of (a) $\lambda_1 = 742$ nm and (b) $\lambda_2 = 782$ nm.

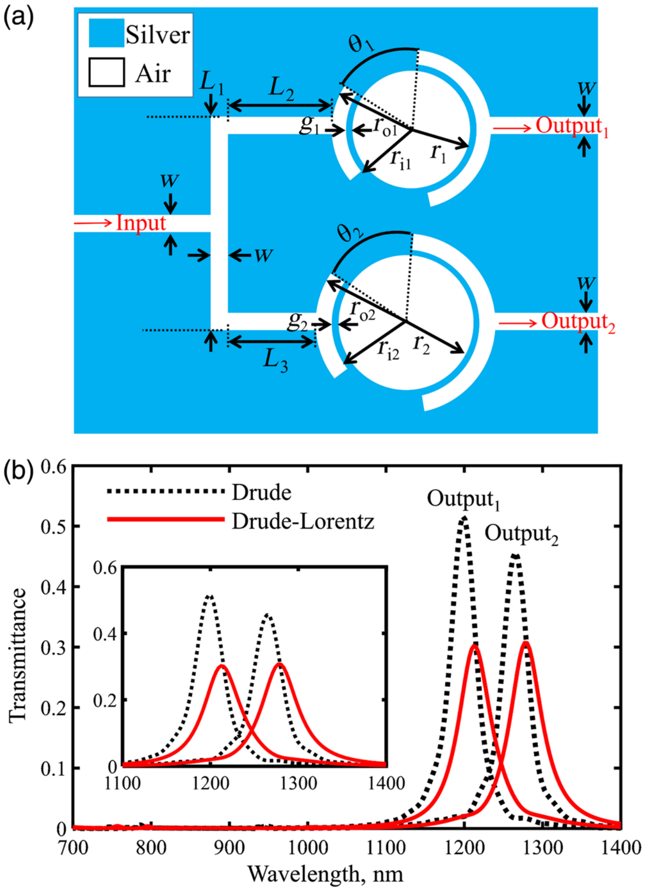

Fig. 7 (a) DeMux2 topology and (b) its transmission spectra.

on the mode orders. For lower mode orders, usually bipolar or unipolar resonances are observed.

Based on filter B [Fig. 1(c)], another two-channel DeMux (DeMux2) is designed, which is shown in Fig. 7(a). The dimensions of DeMux2 are as follows: $r_1 = 310$ nm, $r_2 = 330$ nm, $r_{i1} = 326$ nm, $r_{i2} = 346$ nm, $r_{o1} = 376$ nm, $r_{o2} = 396$ nm, $g_1 = g_2 = 16$ nm, $\theta_1 = \theta_2 = 75$ deg, $w = 50$ nm, $L_1 = 950$ nm, $L_2 = 200$ nm, and $L_3 = 180$ nm. As previously observed, the second improved CNR (a CNR with asymmetric parenthesis-shaped structures) passes the higher wavelength of the initial CNR. Therefore, DeMux2 can generate two resonance modes at higher wavelengths compared with DeMux1. Figure 7(b) shows the transmission spectra of DeMux2 outputs using Drude and DLMs. It can be seen that the resonance wavelengths using DLM for output$_1$ and output$_2$ are $\lambda_1 = 1213$ and $\lambda_2 = 1278$ nm, with maximum transmission peaks of 30% and 31%, respectively; while the maximum transmission peaks with the Drude model are 52% and 46% for wavelengths of $\lambda_1 = 1198$ and $\lambda_2 = 1265$ nm, respectively. To clarify the operating mechanism of DeMux2, the magnetic profile of H_Z for wavelengths of 1213 and 1278 nm are shown in Fig. 8(a) and 8(b), respectively. As seen, the incident light is transmitted to the output$_1$ port for $\lambda_1 = 1213$ nm and output$_2$ port for $\lambda_2 = 1278$ nm, respectively.

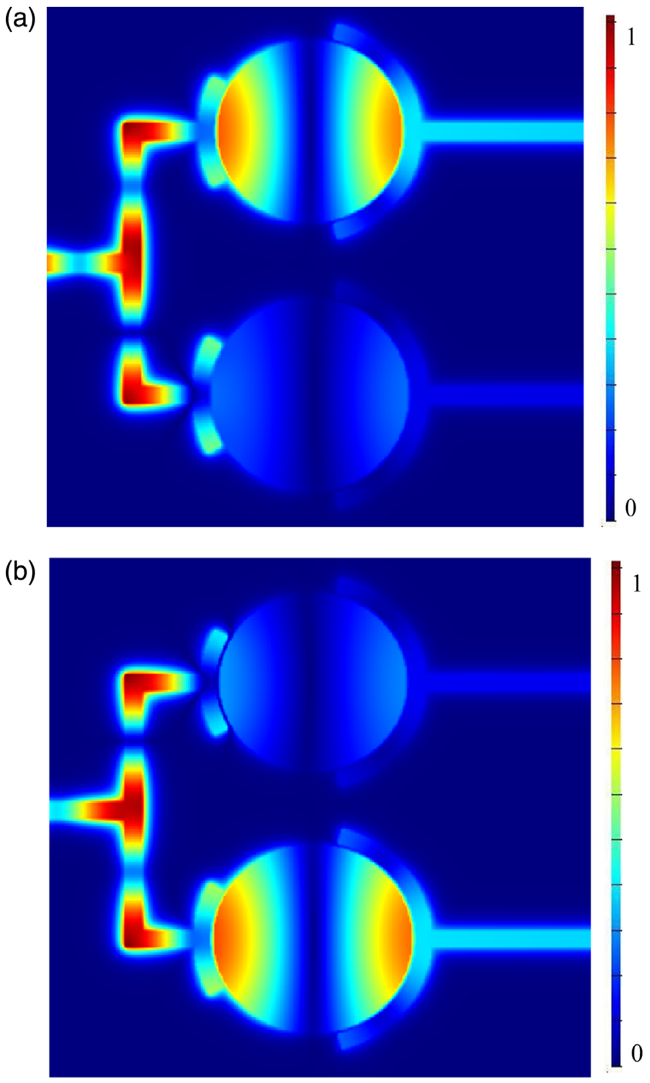

Fig. 8 Field profile of H_Z magnitude of DeMux2 for wavelengths of (a) $\lambda_1 = 1213$ nm and (b) $\lambda_2 = 1278$ nm.

Another method for two-channel DeMux designing is that the two proposed single-mode BPFs be used simultaneously. The topology of the proposed DeMux3 is shown in Fig. 9(a). Here, the dimensions of two improved CNRs are equal. The only difference between them is α degree rotation of the two gaps between the parentheses. The design parameters of DeMux3 are as follows: $r_1 = r_2 = 310$ nm, $r_{i1} = r_{i2} = 326$ nm, $r_{o1} = r_{o2} = 376$ nm, $g_1 = g_2 = 16$ nm, $\theta_1 = \theta_2 = 75$ deg, $w = 50$ nm, $L_1 = 830$ nm, $L_2 = 200$ nm, and $L_3 = 150$ nm. The transmission spectra of two outputs using Drude and DLMs are shown in Fig. 9(b). Using DLM, the resonance wavelengths of $\lambda_1 = 742$ nm and $\lambda_2 = 1213$ nm with the maximum transmission peaks of 31% and 35% are transmitted to the output$_1$ and output$_2$ ports, respectively. The maximum transmission peaks of the resonance wavelengths using the Drude model ($\lambda_1 = 734$ and $\lambda_2 = 1196$ nm) have been increased to 65% and 58%, respectively. As seen from Fig. 9(b), DeMux3 generates two output resonance wavelengths with a far distance from each other. In other words, DeMux3 is composed of two types of improved filters that generate resonance wavelengths at different wavelength ranges.

The magnetic profiles of H_Z for two transmitted wavelengths of DeMux3 ($\lambda_1 = 742$ nm and $\lambda_2 = 1213$ nm) are also shown in Fig. 10(a) and 10(b), respectively. As seen, the wavelengths of 742 and 1213 nm have appeared in the upper and bottom improved CNRs, respectively.

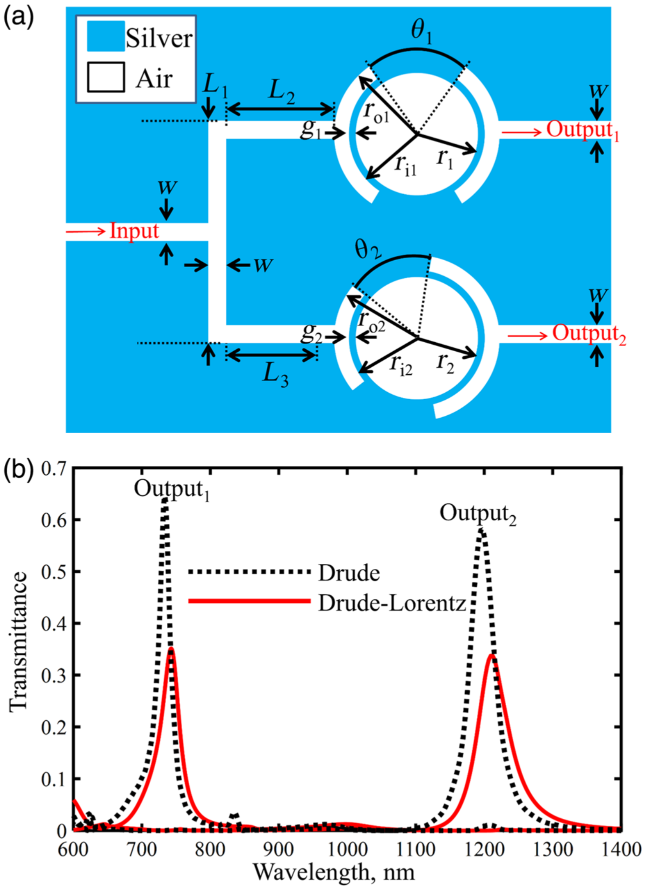

Fig. 9 (a) DeMux3 topology and (b) its transmission spectra.

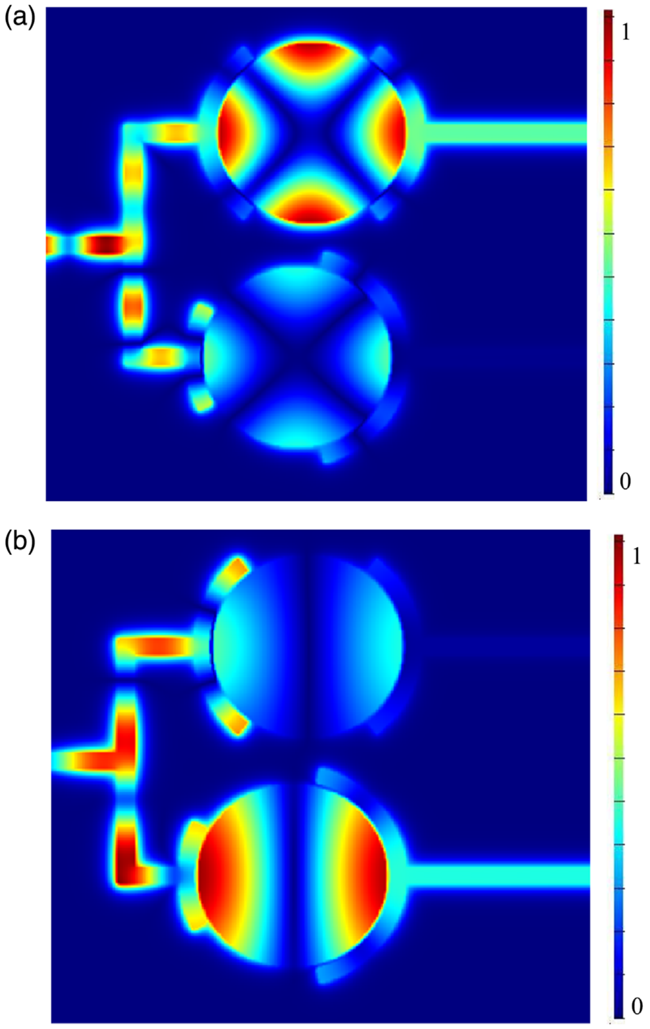

Fig. 10 Field profile of H_Z magnitude of DeMux3 for wavelengths of (a) $\lambda_1 = 742$ nm and (b) $\lambda_2 = 1213$ nm.

4 Triple-Wavelength DeMux Design Procedure

To realize triple-wavelength DeMuxes based on filters A and B, the same procedure is followed in this section. Figure 11(a) shows the topology of a three-channel DeMux using improved CNRs with different dimensions (which is called DeMux4). The dimensions of DeMux4 are as follows: $r_1 = 300$ nm, $r_2 = 330$ nm, $r_3 = 360$ nm, $r_{i1} = 316$ nm, $r_{i2} = 346$ nm, $r_{i3} = 376$ nm, $r_{o1} = 366$ nm, $r_{o2} = 396$ nm, $r_{o3} = 426$ nm, $g_1 = g_2 = g_3 = 16$ nm, $\theta_1 = \theta_2 = \theta_3 = 75$ deg, $w = 50$ nm, $L_1 = 900$ nm, $L_2 = 1400$ nm, $L_3 = 250$ nm, $L_4 = 280$ nm, and $L_5 = 100$ nm. The transmission spectra of three outputs of DeMux4 using Drude and DLMs are shown in Fig. 11(b). It can be seen that the selected wavelengths for output$_1$, output$_2$, and output$_3$ ports are: $\lambda_1 = 716$, $\lambda_2 = 784$, and $\lambda_3 = 842$ nm with maximum transmission peaks of 19%, 28%, and 20%, respectively. However, the maximum transmission peaks of three wavelengths using Drude model ($\lambda_1 = 700$, $\lambda_2 = 775$, and $\lambda_3 = 832$ nm) are 46%, 76%, and 45%, respectively. Due to the use of filter A, DeMux4 generates the three outputs at lower wavelength ranges. As seen in Fig. 12(a), 12(b), and 12(c), respectively in terms of H_Z magnetic profile, the wavelengths of 716, 784, and 842 nm are transmitted to output1, output2, and output3 ports, respectively.

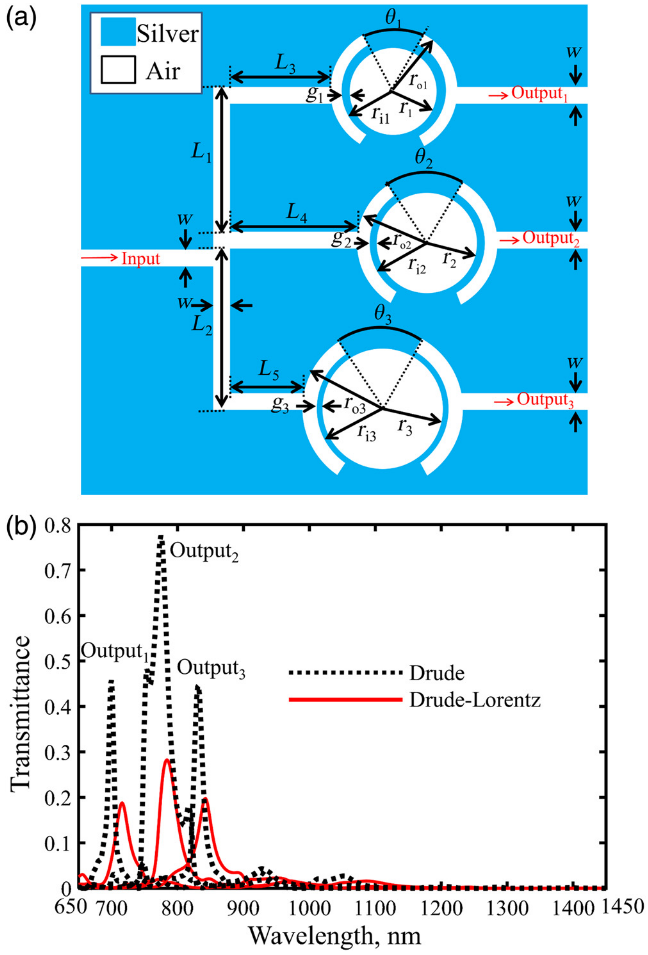

Fig. 11 (a) DeMux4 topology and (b) its transmission spectra.

Another three-channel DeMux (DeMux5) that is designed based on the second improved CNR for higher wavelengths is shown in Fig. 13(a). The dimensions of DeMux5 are as follows: $r_1 = 310$ nm, $r_2 = 330$ nm, $r_3 = 360$ nm, $r_{i1} = 326$ nm, $r_{i2} = 346$ nm, $r_{i3} = 376$ nm, $r_{o1} = 376$ nm, $r_{o2} = 396$ nm, $r_{o3} = 426$ nm, $g_1 = g_2 = g_3 = 16$ nm, $\theta_1 = \theta_2 = \theta_3 = 75$ deg, $w = 50$ nm, $L_1 = 900$ nm, $L_2 = 1300$ nm, $L_3 = 200$ nm, $L_4 = 280$ nm, and $L_5 = 100$ nm.

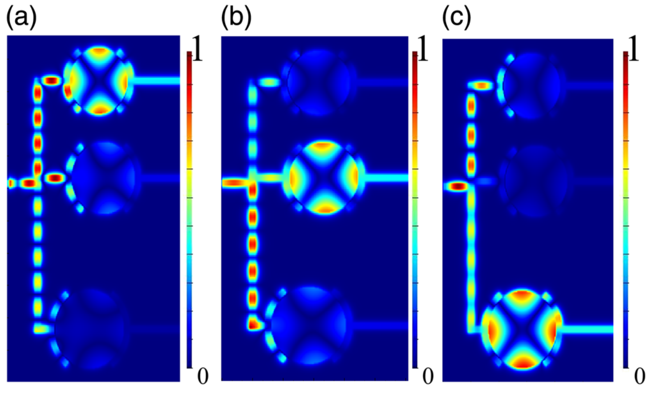

Fig. 12 Field profile of H_Z magnitude of DeMux4 for wavelengths of (a) $\lambda_1 = 716$ nm, (b) $\lambda_2 = 784$ nm, and (c) $\lambda_2 = 842$ nm.

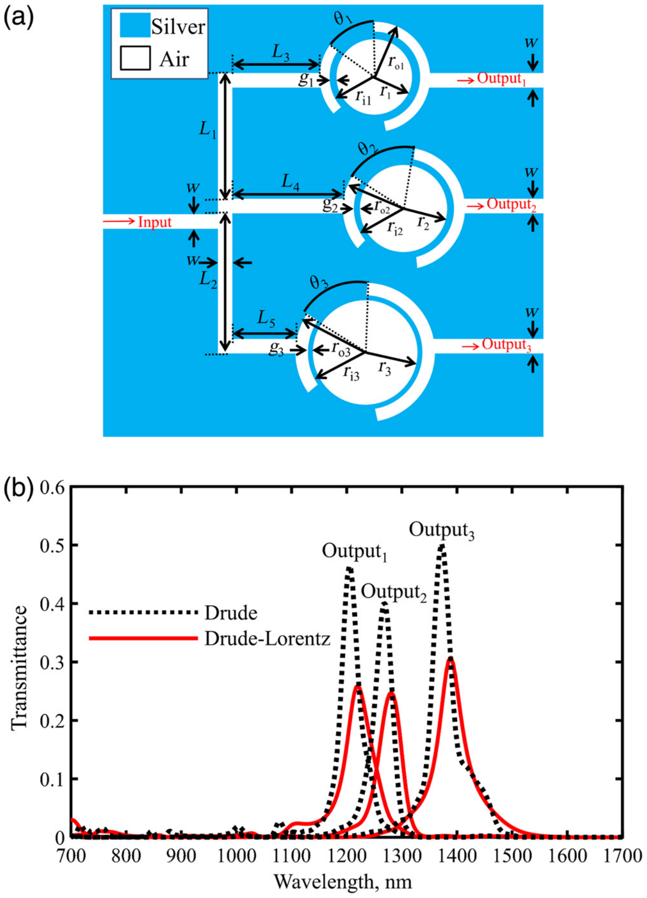

Fig. 13 (a) DeMux5 topology and (b) its transmission spectra.

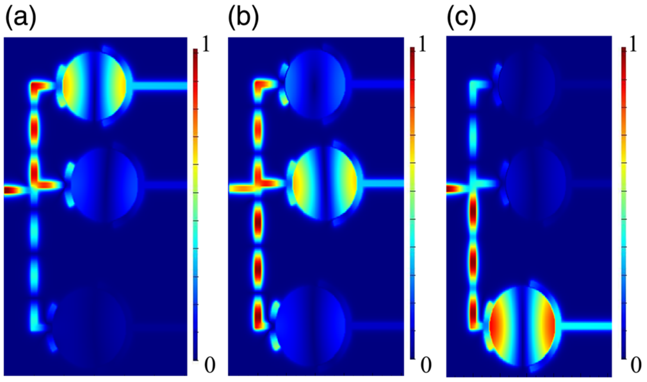

Fig. 14 Field profile of H_Z magnitude of DeMux5 for wavelengths of (a) $\lambda_1 = 1220$ nm, (b) $\lambda_2 = 1281$ nm, and (c) $\lambda_2 = 1389$ nm.

The transmission spectra of the proposed three-channel DeMux are shown in Fig. 13(b). It can be seen from this figure that using three second improved CNRs with nonidentical dimensions, three wavelengths of $\lambda_1 = 1220$, $\lambda_2 = 1281$, and $\lambda_3 = 1389$ nm are transmitted to the output ports. The Drude simulation results generate three wavelengths at $\lambda_1 = 1204$, $\lambda_2 = 1267$, and $\lambda_3 = 1372$ nm. The maximum transmission peaks using Drude and DLMs are 26% and 46% for λ_1, 25% and 40% for λ_2, and 31% and 50% for λ_3, respectively. The magnetic profile of H_Z for DeMux5 is also shown in Fig. 14. As seen, the wavelengths of 1220, 1281, and 1389 nm have appeared in the first, second, and third improved CNRs, respectively (See Fig. 14(a), 14(b), and 14(c).).

Table 2 Performance comparison between the proposed DeMuxes and other works.

Ref.	N	Simulation model	λ_r (nm)	Max. Tr. (%)	FWHM (nm)	Max. Q-factor	Channel spacing (nm)
20	3	Drude	890, 990, 1160	59, 34, 23	24,18, 23	55	135
22	3	Drude	1376, 1444, 1550	56, 60, 69	33, 30, 40	48.13	87
22	5	Drude	1175, 1242, 1378, 1444, 1550	59, 61, 57, 60, 70	18, 27, 24, 30, 40	65.2	94
25	2	Drude	1330, 1487	63, 48.2	75, 74	20.1	157
26	2	Drude	1310, 1550	37, 38	90, 112	14.6	240
29	3	Drude	1140, 1152, 1170	29, 30, 24	12, 13, 13	95	15
DeMux1	2	Drude	734, 774	83, 74	27, 23	33.65	40
		Drude–Lorentz	742, 782	41, 37	41, 33.5	23.35	40
DeMux2	2	Drude	1198, 1265	52, 46	37, 38	33.3	67
		Drude–Lorentz	1213, 1278	30, 31	50, 48	26.63	65
DeMux3	2	Drude	734, 1196	65, 58	18, 41	40.8	462
		Drude–Lorentz	742, 1213	31,35	31, 52	23.94	471
DeMux4	3	Drude	700, 775, 832	46, 76, 45	10, 37, 15	70	66
		Drude–Lorentz	716, 784, 842	19, 28, 20	26, 30, 26	32.4	63
DeMux5	3	Drude	1204, 1267,1372	46, 40, 50	66, 36, 36	38.11	84
		Drude–Lorentz	1220, 1281, 1389	26, 25, 31	54, 46, 53	27.6	85

5 Results and Discussion

The proposed DeMuxes are compared with other works to be able to have a better viewpoint. Table 2 shows the parameters of designed structures along with other published works. These parameters include the number of output channels (N), simulation models, resonance wavelengths (λ_r), maximum transmission peaks at resonance wavelengths (Max. Tr.), full width at half maximums (FWHM), maximum quality factor of resonance wavelengths (Max. Q-factor), and channel spacing. The amount of the channel spacing is the average of the channel spacings for each DEMUX. This is due to the fact that such DEMUXes have nonidentical channel spacings.

As previously mentioned, the Drude model is an approximated model that is used in the most studies. Hence, the results obtained from this model are not reliable. To be able to compare our results with those reported in the literature, we have also repeated the simulations using the Drude model. As can be seen, when using the Drude model better parameters such as Max. Tr., FWHM, and Max. Q-factor have been observed. Also, the channel spacings of the proposed DEMUXes are almost on a same order of magnitude with other works.

6 Conclusion

Using improved CNRs, two single-mode plasmonic BPFs have been designed. The CNRs are coupled with symmetric and asymmetric parenthesis-shaped structures, respectively. The parenthesis-shaped structures not only create single-mode filters, but also increase the maximum transmission peaks, which are very desirable for designing DeMuxes. Based on such single-mode filters, different structures for two and three channel DeMuxes have been proposed. By tuning the improved CNR dimensions, different DeMux structures were obtained. All devices were numerically simulated using the FDTD method, where the silver metal is characterized by Drude and DLMs. The proposed DeMuxes can be used in the nanophotonic integrated circuits.

Acknowledgments

The authors would also like to thank the reviewers for their valuable comments. On behalf of all the authors, the corresponding author states that there is no conflict of interest.

References

1. W. L. Barnes, A. Dereux, and T. W. Ebbesen, "Surface plasmon subwavelength optics," *Nature* **424**(6950), 824–830 (2003).
2. S. A. Maier, *Plasmonics: Fundamentals and Applications*, Springer Science and Business Media, Berlin, Germany (2007).
3. M. Danaie and H. Kaatuzian, "Design of a photonic crystal differential phase comparator for a Mach-Zehnder switch," *J. Opt.* **13**(1), 015504 (2010).
4. A. Dideban, H. Habibiyan, and H. Ghafoorifard, "Photonic crystal channel drop filter based on ring-shaped defects for DWDM systems," *Physica E* **87**, 77–83 (2017).
5. M. R. Rakhshani and M. A. Mansouri-Birjandi, "Realization of tunable optical filter by photonic crystal ring resonators," *Optik* **124**, 5377–5380 (2013).
6. M. Danaie, R. N. Far, and A. Dideban, "Design of a high-bandwidth Y-shaped photonic crystal power splitter for TE modes," *Int. J. Opt. Photonics* **12**(1), 33–42 (2018).
7. A. Geravand, M. Danaie, and S. Mohammadi, "All-optical photonic crystal memory cells based on cavities with a dual-argument hysteresis feature," *Opt. Commun.* **430**, 323–335 (2019).
8. M. Danaie and B. Kiani, "Design of a label-free photonic crystal refractive index sensor for biomedical applications," *Photonics Nanostruct. Fundam. Appl.* **31**, 89–98 (2018).
9. M. Moradi, M. Danaie, and A. A. Orouji, "Design and analysis of an optical full-adder based on nonlinear photonic crystal ring resonators," *Optik* **172**, 127–136 (2018).
10. M. Danaie, A. Geravand, and S. Mohammadi, "Photonic crystal double-coupled cavity waveguides and their application in design of slow-light delay lines," *Photonic Nanostruct.* **28**, 61–69 (2018).
11. D. K. Gramotnev and S. I. Bozhevolnyi, "Plasmonics beyond the diffraction limit," *Nat. Photonics* **4**(2), 83–91 (2010).
12. S. I. Bozhevolnyi et al., "Channel plasmon subwavelength waveguide components including interferometers and ring resonators," *Nature* **440**(7083), 508–511 (2006).
13. S. Khani, M. Danaie, and P. Rezaei, "Realization of single-mode plasmonic bandpass filters using improved nanodisk resonators," *Opt. Commun.* **420**, 147–156 (2018).
14. M. Zavvari, M. T. H. Azar, and A. Arashmehr, "Tunable band-stop plasmonic filter based on square ring resonators in a metal-insulator-metal structure," *J. Mod. Opt.* **64**(20), 2221–2227 (2017).
15. S. Khani, M. Danaie, and P. Rezaei, "Design of a single-mode plasmonic bandpass filter using a hexagonal resonator coupled to graded-stub waveguides," *Plasmonics* 1–10 (2018).
16. H. Arianfard, B. Khajeheian, and R. Ghayour, "Tunable band (pass and stop) filters based on plasmonic structures using Kerr-type nonlinear rectangular nanocavity," *Opt. Eng.* **56**, 121902 (2016).
17. L. Chen et al., "Numerical analysis of a near-infrared plasmonic refractive index sensor with high figure of merit based on a fillet cavity," *Opt. Express* **24**(9), 9975–9983 (2016).
18. M. R. Rakhshani and M. A. Mansouri-Birjandi, "High-sensitivity plasmonic sensor based on metal–insulator–metal waveguide and hexagonal-ring cavity," *IEEE Sens. J.* **16**(9), 3041–3046 (2016).
19. M. R. Rakhshani and M. A. Mansouri-Birjandi, "High sensitivity plasmonic refractive index sensing and its application for human blood group identification," *Sens. Actuators B* **249**, 168–176 (2017).
20. M. R. Rakhshani and M. A. Mansouri-Birjandi, "Utilizing the metallic nano-rods in hexagonal configuration to enhance sensitivity of the plasmonic racetrack resonator in sensing application," *Plasmonics* **12**, 999–1006 (2017).
21. C. H. Chen and K. S. Liao, "1xN plasmonic power splitters based on metal-insulator-metal waveguides," *Opt. Express* **21**(4), 4036–4043 (2013).
22. D. Xiang and W. Li, "MIM plasmonic waveguide splitter with tooth-shaped structures," *J. Mod. Opt.* **61**(3), 222–226 (2014).
23. A. N. Taheri and H. Kaatuzian, "Design and simulation of a nanoscale electro-plasmonic 1×2 switch based on asymmetric metal–insulator–metal sub filters," *Appl. Opt.* **53**(28), 6546–6553 (2014).
24. A. N. Taheri and H. Kaatuzian, "Numerical investigation of a nano-scale electro-plasmonic switch based on metal–insulator–metal stub filter," *Opt. Quantum Electron.* **47**(2), 159–168 (2015).
25. W. Zhao and Z. Lu, "Nanoplasmonic optical switch based on Ga-Si_3N_4-Ga waveguide," *Opt. Eng.* **50**, 074002 (2011).
26. M. Ayata et al., "High-speed plasmonic modulator in a single metal layer," *Science* **358**(6363), 630–632 (2017).
27. A. Khaleque and H. T. Hattori, "Plasmonic electro-absorption modulator and polarization selector," *J. Mod. Opt.* **64**(12), 1164–1174 (2017).
28. C. Li et al., "Wideband slow light based on plasmon-induced transparency at telecom frequency," *Opt. Commun.* **351**, 26–29 (2015).
29. S. Kumar, L. Singh, and N. K. Chen, "All-optical bit magnitude comparator device using metal–insulator–metal plasmonic waveguide," *Opt. Eng.* **56**, 121908 (2017).
30. M. R. Rakhshani and M. A. Mansouri-Birjandi, "Design and simulation of wavelength demultiplexer based on heterostructure photonic crystals ring resonators," *Physica E* **50**, 97–101 (2013).
31. M. A. Mansouri-Birjandi and M. R. Rakhshani, "A new design of tunable four-port wavelength demultiplexer by photonic crystal ring resonators," *Optik* **124**, 5923–5926 (2013).
32. M. R. Rakhshani and M. A. Mansouri-Birjandi, "Heterostructure four channel wavelength demultiplexer using square photonic crystals ring resonators," *J. Electromagn. Waves Appl.* **26**, 1700–1707 (2012).
33. M. R. Rakhshani and M. A. Mansouri-Birjandi, "Design and simulation of four-channel wavelength demultiplexer based on photonic crystal circular ring resonators for optical communications," *J. Opt. Commun.* **35**, 9–15 (2014).
34. M. R. Rakhshani, M. A. Mansouri-Birjandi, and Z. Rashki, "Design of six channel demultiplexer by heterostructure photonic crystal resonant cavity," *Int. Res. J. Appl. Basic Sci.* **4**, 976–984 (2013).
35. M. R. Rakhshani and M. A. Mansouri-Birjandi, "Wavelength demultiplexer using heterostructure ring resonators in triangular photonic crystals," *Indones. J. Electr. Eng. Comput. Sci.* **11**, 1721–1724 (2013).
36. F. Lu et al., "A compact wavelength demultiplexing structure based on arrayed MIM plasmonic nano-disk cavities," *Opt. Commun.* **285**(24), 5519–5523 (2012).
37. F. Lu et al., "A plasmonic triple-wavelength demultiplexing structure based on a MIM waveguide with side-coupled nanodisk cavities," *IEEE Trans. Nanotechnol.* **12**(6), 1185–1190 (2013).
38. H. Liu et al., "A T-shaped high resolution plasmonic demultiplexer based on perturbations of two nanoresonators," *Opt. Commun.* **334**, 164–169 (2015).

39. G. Wang et al., "Tunable multi-channel wavelength demultiplexer based on MIM plasmonic nanodisk resonators at telecommunication regime," *Opt. Express* **19**(4), 3513–3518 (2011).
40. M. R. Rakhshani and M. A. Mansouri-Birjandi, "Dual wavelength demultiplexer based on metal–insulator–metal plasmonic circular ring resonators," *J. Mod. Opt.* **63**(11), 1078–1086 (2016).
41. Z. Zhang et al., "Plasmonic filter and demultiplexer based on square ring resonator," *Appl. Sci.* **8**(3), 462 (2018).
42. Q. Chen, Y. Wang, and Y. Wu, "Integer-programming model for plasmonic waveguide demultiplexers," *Plasmonics* **10**(2), 329–334 (2015).
43. N. Nozhat and N. Granpayeh, "Analysis of the plasmonic power splitter and MUX/DEMUX suitable for photonic integrated circuits," *Opt. Commun.* **284**(13), 3449–3455 (2011).
44. X. M. Geng et al., "Tunable plasmonic wavelength demultiplexing device using coupled resonator system," *IEEE Photonics J.* **8**(3), 1–8 (2016).
45. C. Zhao et al., "High-resolution compact plasmonic wavelength demultiplexers based on cascading square resonators," *Chin. Phys. Lett.* **30**(5), 054212 (2013).
46. X. Mei et al., "A wavelength demultiplexing structure based on plasmonic MDM side-coupled cavities," *J. Opt. Soc. Am. B* **27**(12), 2707–2713 (2010).
47. A. B. Ayoub and M. A. Swillam, "High performance optical systems using MIM based plasmonic structures," *J. Phys. Commun.* **1**(3), 035007 (2017).
48. A. Rahimzadegan, N. Granpayeh, and S. P. Hosseini, "Improved plasmonic filter, ultra-compact demultiplexer, and splitter," *J. Opt. Soc. Korea* **18**(3), 261–273 (2014).
49. A. Rahimzadegan, S. P. Hosseini, and K. Qaderi, "Improved plasmonic demultiplexer based on tapered and rectangular slot MIM waveguide," *Int. J. Electron. Commun. Eng.* **7**(5), 506–510 (2013).
50. Y. Y. Xie et al., "Theoretical investigation of a plasmonic demultiplexer in MIM waveguide crossing with multiple side-coupled hexagonal resonators," *IEEE Photonics J.* **8**(5), 1–12 (2016).
51. M. T. Azar et al., "Design of a high-performance metal–insulator–metal plasmonic demultiplexer," *J. Nanophotonics* **11**(2), 026002 (2017).
52. A. Noual et al., "Modeling of two-dimensional nanoscale y-bent plasmonic waveguides with cavities for demultiplexing of the telecommunication wavelengths," *New J. Phys.* **11**(10), 103020 (2009).
53. J. H. Zhu et al., "A nanometeric plasmonic wavelength demultiplexer based on a T-shaped waveguide structure with double teeth-shaped waveguide at telecommunication wavelengths," *J. Mod. Opt.* **57**(21), 2154–2158 (2010).
54. S. Khani and M. Hayati, "Compact microstrip lowpass filter with wide stopband and sharp roll-off," *Microwave J.* **60**(11), 86–92 (2017).
55. S. Khani et al., "Adjustable compact dual-band microstrip bandpass filter using T-shaped resonators," *Microwave Opt. Technol. Lett.* **59**(12), 2970–2975 (2017).
56. S. Khani et al., "Tunable compact microstrip dual-band bandpass filter with tapered resonators," *Microwave Opt. Technol. Lett.* **60**(5), 1256–1261 (2018).
57. S. Khani, M. Danaie, and P. Rezaei, "Miniaturized microstrip dual-band bandpass filter with wide upper stop-band bandwidth," *Analog Integr. Circuits Signal Process.* 1–10 (2018).
58. C. E. Saavedra, "Microstrip multiplexer with compact in-line feed structure," *Microwave Opt. Technol. Lett.* **49**(12), 3128–3130 (2007).
59. P. H. Deng, B. L. Huang, and B. L. Chen, "Designs of microstrip four- and five-channel multiplexers using branch-line-shaped matching circuits," *IEEE Trans. Compon. Packag. Manuf. Technol.* **5**(9), 1331–1338 (2015).
60. A. Valizade, P. Rezaei, and A. A. Orouji, "Design of reconfigurable active integrated microstrip antenna with switchable low-noise amplifier/power amplifier performances for wireless local area network and WiMAX applications," *IET Microwaves Antennas Propag.* **9**(9), 872–881 (2015).
61. M. Borhani, P. Rezaei, and A. Valizade, "Design of a reconfigurable miniaturized microstrip antenna for switchable multiband systems," *IEEE Antennas Wirel. Propag. Lett.* **15**, 822–825 (2016).
62. H. Y. Li et al., "Analysis of the Drude model in metallic films," *Appl. Opt.* **40**(34), 6307–6311 (2001).
63. E. D. Palik, *Handbook of Optical Constants of Solids*, Academic Press, San Diego (1998).
64. B. Liu et al., "Rotation and conversion of transmission mode based on a rotatable elliptical core ring resonator," *Opt. Commun.* **369**, 44–49 (2016).
65. H. Lu et al., "Tunable band-pass plasmonic waveguide filters with nanodisk resonators," *Opt. Express* **18**(17), 17922–17927 (2010).
66. A. Dolatabady, N. Granpayeh, and V. F. Nezhad, "A nanoscale refractive index sensor in two dimensional plasmonic waveguide with nanodisk resonator," *Opt. Commun.* **300**, 265–268 (2013).
67. Z. Yu et al., "Integrated tunable optofluidics optical filter based on MIM side-coupled-cavity waveguide," *Plasmonics* **7**(4), 603–607 (2012).

Shiva Khani received her BSc degree in electronic engineering from Razi University in 2011 and her MSc degree in electronic engineering from Islamic Azad University, Science and Research Branch, Kermanshah, Iran, in 2014. Currently, she is working toward her PhD in electronics engineering at Semnan University. She has published several papers in different journals. Her research interests include plasmonics devices and microwave circuits.

Mohammad Danaie received his bachelor's and master's degrees from Ferdowsi University of Mashhad in 2005 and 2007, respectively, with honors and his PhD from Amirkabir University of Technology, Tehran, Iran, in 2011, all in electrical engineering. He has been an assistant professor of electrical engineering at Semnan University, Semnan, Iran, since 2012. His current research interests include integrated all-optical devices, photonic crystals, surface plasmons, and nanophotonic devices.

Pejman Rezaei received his BS degree in communication engineering from communication faculty, Tehran, Iran, in 2000, and his MS and PhD degrees from Tarbiat Modarres University, Tehran, Iran, in 2002 and 2007, respectively. His current research interests are electromagnetics theory, antennas, bioelectomagnetics, wave propagation, and satellite communication. Currently, he is an associate professor at Semnan University, Semnan, Iran.